nature astronomy

LETTERS

https://doi.org/10.1038/s41550-017-0289-8

Powering prolonged hydrothermal activity inside Enceladus

Gaël Choblet[1*], Gabriel Tobie[1], Christophe Sotin[2], Marie Běhounková[3], Ondřej Čadek[3], Frank Postberg[4,5] and Ondřej Souček[6]

Geophysical data from the Cassini spacecraft imply the presence of a global ocean underneath the ice shell of Enceladus[1], only a few kilometres below the surface in the South Polar Terrain[2–4]. Chemical analyses indicate that the ocean is salty[5] and is fed by ongoing hydrothermal activity[6–8]. In order to explain these observations, an abnormally high heat power (>20 billion watts) is required, as well as a mechanism to focus endogenic activity at the south pole[9,10]. Here, we show that more than 10 GW of heat can be generated by tidal friction inside the unconsolidated rocky core. Water transport in the tidally heated permeable core results in hot narrow upwellings with temperatures exceeding 363 K, characterized by powerful (1–5 GW) hotspots at the seafloor, particularly at the south pole. The release of heat in narrow regions favours intense interaction between water and rock, and the transport of hydrothermal products from the core to the plume sources. We are thus able to explain the main global characteristics of Enceladus: global ocean, strong dissipation, reduced ice-shell thickness at the south pole and seafloor activity. We predict that this endogenic activity can be sustained for tens of millions to billions of years.

Tidal dissipation within the ice of Enceladus is too weak to counterbalance the global heat loss from the ocean by thermal diffusion through the ice shell (20–25 GW)[2]. Although enhanced tidal dissipation in the ice shell could sustain the activity in the South Polar Terrain (SPT) owing to its reduced thickness at those latitudes and to the presence of active faults[11,12], the absence of additional heat sources would nevertheless lead to the overall crystallization of the internal ocean in less than 30 Myr[2]. This suggests that another dissipation process provides the missing heating power deeper in the moon's interior, possibly in the core.

The estimated core density of Enceladus (see Methods) is low for a metal–rock core, requiring considerable (water-filled) porosity and a composition dominated by iron-bearing hydrated minerals whose abundance dictates the core water content. For iron numbers (Fe/(Fe + Mg)) between 50% and 100% of the chondritic value, the porosity of a core composed primarily of hydrated silicates would be 20–30% (see Methods). If anhydrous minerals are still present, as suggested by the recent detection of hydrogen in the plume[8], porosities are slightly larger. Owing to low confining pressures (<40 MPa) and moderate temperatures reached in the core, such an elevated porosity inherited from the accretion process[13,14] may be maintained over geological timescales[15]. Moreover, the joint action of thermochemical and tidal stresses as well as hydrothermalism may sustain the core in a highly fragmented or unconsolidated state.

A core with high porosity inside Enceladus may be subjected to considerable tidal heating, at least during some period of time[16,17]. Previous work[17] quantified the rate of dissipation for an ice-filled porous rock core, but did not consider the tidal dissipation once ice melting occurs. Other authors[16] investigated the consequences of strong tidal dissipation on the heat transfer by water flow in a porous permeable core, but they considered uniform and arbitrary values of tidal dissipation and limited their analysis to two-dimensional (2D) geometry. Here we perform coupled simulations of tidal friction and heat transfer in a porous water-filled core using a 3D approach.

In absence of direct constraints on the mechanical properties of Enceladus' core, we consider a wide range of parameters to characterize the rate of tidal friction and the efficiency of water transport by porous flow. The unconsolidated core of Enceladus can be viewed as a highly granular/fragmented material, in which tidal deformation is likely to be associated with intergranular friction during fragment rearrangements (see Methods). Although this mechanism depends on microstructure characteristics unknown in the case of Enceladus, the mechanical response of such unconsolidated media is usually parameterized using the effective shear modulus and the dissipation function. These two parameters control the response amplitude to cyclic forcing and the fraction of mechanical energy that is converted into heat, respectively[18]. The local dissipation rate is computed from the strain and stress tensors, and the global dissipation power is evaluated by integrating the dissipation rate over the entire satellite (see Methods). A total power of 10 to 30 GW can be generated for effective shear modulus ranging between 10^7 and 10^8 Pa and dissipation function between 0.2 and 0.8 (Fig. 1a and Supplementary Fig. 1). Such low values of effective shear modulus associated with high dissipation could be explained by weakening effects due to cyclic tidal strain, in a similar way to what is observed in cyclic loading tests on saturated sand and gravel mixtures in the laboratory (see Methods). Such a highly dissipative core may partly explain the observed lag in plume activity[19–21]. However, existing mechanical tests are performed at frequencies higher than tidal forcing and pressures lower than core pressure. Extrapolation to Enceladus conditions will have to be confirmed by dedicated experiments.

The degree-two shape of the tidal potential results in a modulation of tidal heating as a function of latitude and longitude

[1]Laboratoire de Planétologie et Géodynamique, UMR-CNRS 6112, Université de Nantes, 44322 Nantes Cedex 03, France. [2]Jet Propulsion Laboratory, Caltech, 4800 Oak Grove Drive, Pasadena, CA 91109, USA. [3]Charles University, Department of Geophysics, V Holešovičkách 2, 180 00 Praha 8, Czech Republic. [4]Institut für Geowissenschaften, Universität Heidelberg, Im Neuenheimer Feld 236, 69120 Heidelberg, Germany. [5]Klaus-Tschira-Labor für Kosmochemie, Universität Heidelberg, Im Neuenheimer Feld 236, 69120 Heidelberg, Germany. [6]Charles University, Mathematical Institute, Sokolovská 83, 186 75 Praha 8, Czech Republic. *e-mail: gael.choblet@univ-nantes.fr

© 2017 Macmillan Publishers Limited, part of Springer Nature. All rights reserved.

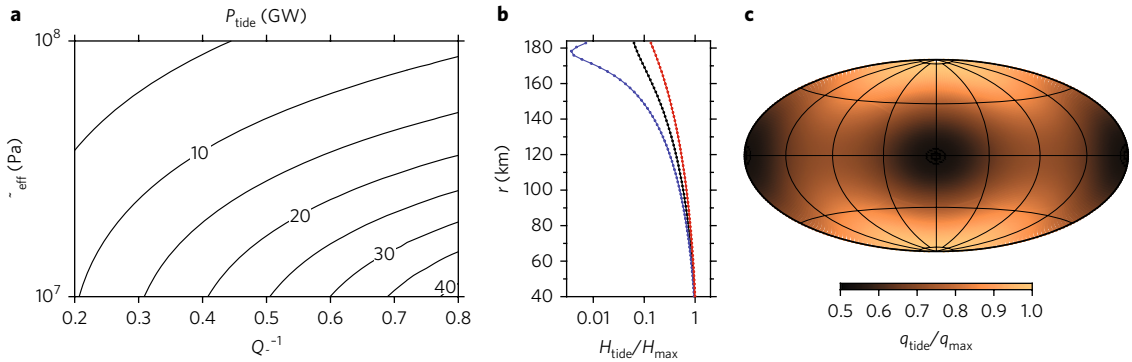

Fig. 1 | Tidal friction in the porous core of Enceladus saturated with liquid water. a, Total power generated in the core (contours in GW) as a function of effective shear modulus μ_{eff} and dissipation function Q_μ^{-1}. **b**, Average (black), minimum (blue) and maximum (red) heating rate H_{tide} at a given radius. Values are normalized by the maximum rate obtained at the smallest radius H_{max} ($H_{max} = 2.4 \times 10^{-6}$ W m^{-3} for $P_{tide} = 20$ GW). **c**, Spatial distribution of 'tidal heat flux' q_{tide} (radial integration of volumetric heating rate H_{tide} at each location) normalized by the maximum (polar) value (q_{max}).

(see Methods). These variations are small near the core centre where heat production is maximal (Fig. 1b), but they increase toward the core surface. This leads to integrated heating at the poles that is twice that at the equator at the sub-Saturnian and anti-Saturnian points (Fig. 1c). To determine the consequences of such a heterogeneous heat production on the internal dynamics of Enceladus' core, we simulate the Darcy flow of liquid water in a 3D spherical porous rock medium and systematically investigate plausible ranges for the three controlling parameters: permeability (K), global power dissipated in the core (P_{tide}) and porosity (φ) (see Methods).

In our simulations, flow and temperature fields both exhibit localized linear upwellings of hot water interspaced with colder regions of passive downward water flux, a heat pipe mechanism typically obtained for convection with a permeable surface[22]. Cool liquid water from the ocean enters the core passively and is gradually heated as it penetrates deeper in regions of reduced gravity (Supplementary Fig. 5). There, narrow hot sheets form, losing little of their heat as they actively rise with increasing buoyancy. Their temperature and velocity are mostly determined by the assumed permeability and total dissipated power (Fig. 2). Although much larger thermal anomalies develop for low K values, the severe decrease in associated velocity results in smaller mass flux and heat power advected out of the core (see Supplementary Section S2.3 and Supplementary Fig. 8).

The detection of nanometre-sized silica particles originating from Enceladus is consistent with water–rock interactions at moderately high temperature (~363 K for pH > 9.5)[6,7]. Our simulations show that the core permeability should be lower than 10^{-12} m^2 in order to induce temperatures exceeding 363 K (Fig. 2 and Supplementary Fig. 6). Conversely, values as small as 10^{-15} m^2 lead to low mass flux and high water temperatures, possibly exceeding the boiling point for high dissipation rate. The boiling point represents the upper temperature limit of our model's validity, as it does not allow us to consistently capture the associated phase change (see Methods for details). In the following, we consider permeability values ranging between 10^{-14} and 10^{-13} m^2, corresponding to a good compromise in terms of vent temperatures and outflow.

Heat flux distribution through the core–ocean interface is dominated by radial advection of water with lateral temperature variations. In a set of models with homogeneous heating, it is found to depend strongly on permeability and global heat power: smaller-scale and time-dependent slowly drifting patterns correspond to larger K and P_{tide} values (Fig. 3 and Supplementary Fig. 7). Even though tidal dissipation presents a relatively diffuse lateral heterogeneity with moderate amplitude (Fig. 1), it suffices

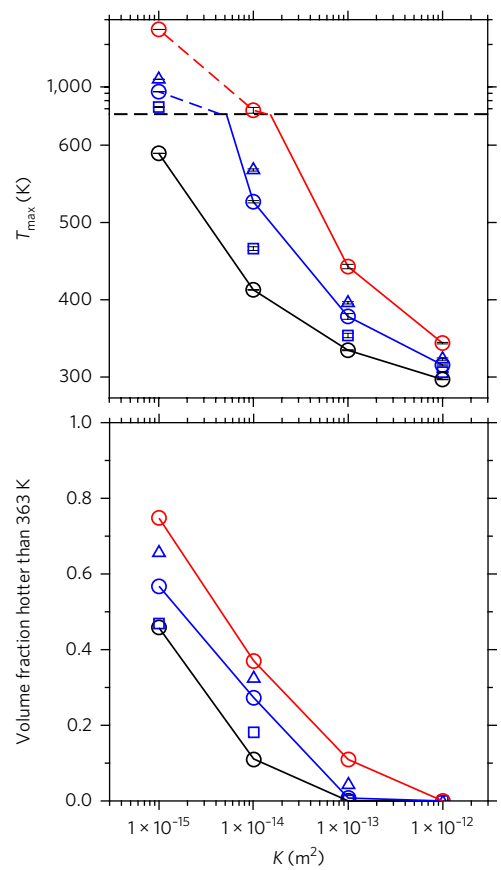

Fig. 2 | Synthetic characteristics for porous convection of liquid water with heterogeneous tidal heating of the rocky core. Maximum temperature T_{max} (top) and volume fraction above 363 K (bottom) are shown as a function of permeability K. Colours denote the global tidal power P_{tide}: 3 GW (black), 10 GW (blue) and 30 GW (red). Symbols indicate porosity φ: 0.1 (squares), 0.2 (circles) and 0.3 (triangles). Cases with $\varphi = 0.1$ and 0.2 are displayed only for $P_{tide} = 10$ GW. Vertical bars denote the range of values obtained in time-dependent simulations. Note that, in the case of T_{max}, two different scales (linear/log) are used for temperature with the dashed horizontal line approximately indicating the boiling point.

to focus upwellings of hot liquid water into a narrow annulus (Fig. 3) coinciding with the maximum heating. Maximum upward advection is permanently anchored at the poles, characterized

© 2017 Macmillan Publishers Limited, part of Springer Nature. All rights reserved.

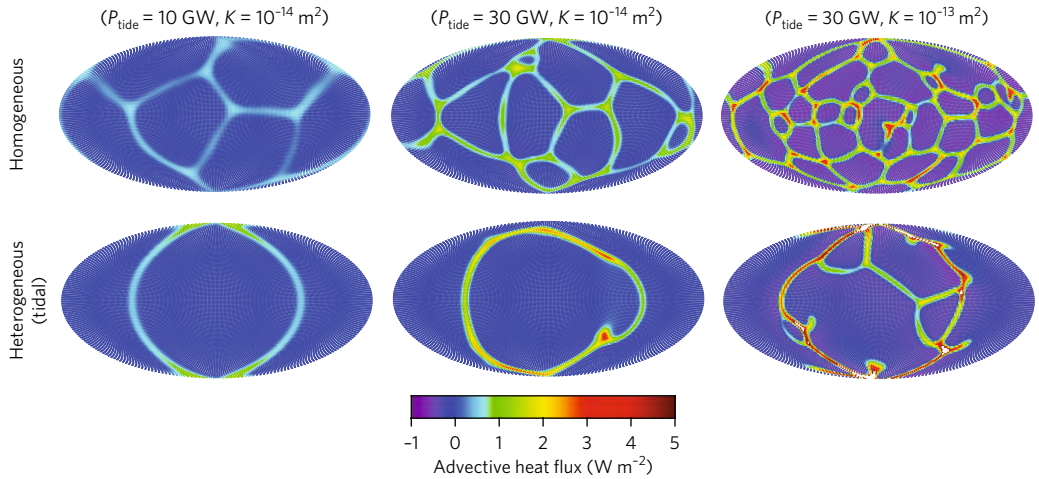

Fig. 3 | Heat flux pattern at the interface between rocky core and ocean. Advective flux distribution through the surface of the porous core: three sets of parameters are presented for both homogeneous and heterogeneous (tidal) volumetric heating. Porosity is 0.2 for all these examples.

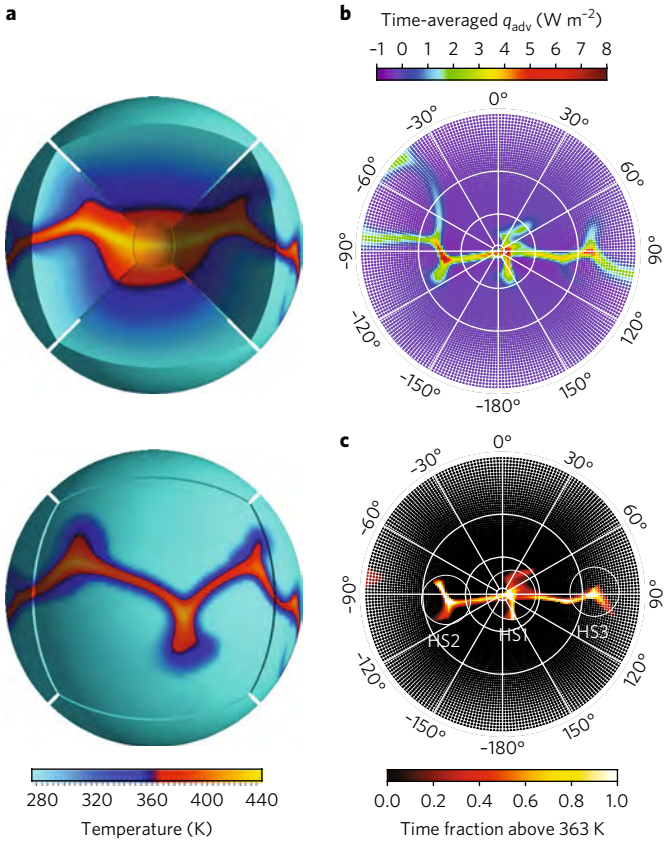

Fig. 4 | Hotpots at the seafloor. a, South polar view of the temperature field obtained for a case with $P_{tide} = 30$ GW, $K = 10^{-13}$ m^2, $\varphi = 0.2$. In the upper panel, one of the six blocks from the mesh is removed to reveal the inner temperature field. The colour scale is nonlinear in order to highlight the specific role of isotherm 363 K. **b**, Advective heat flux at the rocky core/ocean interface averaged over a period of 10 Myr (stereographic projection). The typical averaged net power outputs in the three main hotspots identified in the southern hemisphere in this example are 5.6 GW (HS1), 3.2 GW (HS2) and 1.3 GW (HS3). **c**, Time fraction during which a given location at the rocky core/ocean interface remains at a temperature above 363 K (stereographic projection). The duration of this time-dependent simulation is 10 Myr.

by a few hotspots releasing a power ranging between 1 and 10 GW and stable for at least 10 Myr (Fig. 4).

Although Enceladus' ocean dynamics probably involve large-scale turbulence (either of convective origin[23] or caused by tidal forcing[24]) shaping the exchanges between the deep interior and the ice shell at the global scale, such hot water outflows from the core are expected to produce smaller-scale hydrothermal plumes that locally affect the ice shell above. Scaling analysis indicates that seafloor hotspots releasing a power of 5 GW (Fig. 4) generate ocean plumes with a vertical velocity of a few centimetres per second (see Methods). Materials carried by these thermal vents, such as nanometre-sized silica particles, would be transported from the seafloor to the ice–ocean interface on timescales of a few weeks to months, consistent with their limited growth inferred from Cassini[6,7].

The predominance of heat release under the poles is consistent with an ice-shell structure presenting minimal thicknesses in polar regions[2]. The observed difference between the north and south of Enceladus cannot be attributed to the deep processes as simulated here (see Supplementary Section 2.4 and Supplementary Figs. 7 and 9). A difference in the mechanical response of the ice shell between the two poles due to thinner and more deformable shell at the south would, however, create a north–south asymmetry in heat production in the core (not prescribed explicitly in the models presented here; see Methods, Supplementary Section 1 and Supplementary Fig. 2). This effect would be further enhanced by the amplifications of tidal friction along the SPT faults when the shell becomes thinner than 5–10 km (refs [11,12]), thus possibly explaining a thermal runaway in this region. Moreover, the maximum hot water outflow along two specific meridians in all models, regardless of the latitude, is also consistent with a thinner ice shell predicted in two regions centred on these longitudes[2].

We show that, for $K < 10^{-12}$ m^2, hydrothermal activity would occur as long as a power of at least 10 GW is produced in the core. But for how long can such a power be generated? This first depends on how the orbital eccentricity evolves through time, which is determined by the dissipation rate within Saturn and the strength of the orbital resonance with the moon Dione. The latest estimate of Saturn's tidal dissipation[25] is considerably higher than classically anticipated and yields an equilibrium heating $P_{tide} > 10$ GW for which the present-day eccentricity remains constant through time. Tidal evolution assuming resonance locking and internal oscillation modes in Saturn could even maintain an orbital equilibrium for $P_{tide} = 50$ GW (ref. [26]): hydrothermal activity would then persist for billions of years.

© 2017 Macmillan Publishers Limited, part of Springer Nature. All rights reserved.

A large decrease in P_{tide} is predicted in the case of ocean crystallization (see Supplementary Fig. 2) so that a second requirement is that the ocean remains present at a global scale. This is guaranteed by the global diffusive heat equilibrium for $P_{tide} > 15$ GW. For $P_{tide} \approx 10$–15 GW, this equilibrium predicts an average ice shell of 35–40 km: in the case of considerable lateral variations, direct contact might occur between the porous core and the ice in its thickest equatorial regions, at the sub-Saturnian and anti-Saturnian points, possibly causing the cessation of hydrothermalism. A minimal timescale before such a low dissipative state is reached is determined by the local thermal diffusion flux through the ice (~15–20 mW m^{-2})[2]. Neglecting probable lateral ice flow that will reduce the growth rate of icy roots, this timescale is already ~20 Myr, which can be considered as a very conservative minimal duration when hydrothermal activity is sustained in the core.

Our simulations indicate that, for $10^{-14} < K < 10^{-13}$ m^2, the entire ocean is processed in the core at temperatures higher than 363 K in 25–250 Myr (Supplementary Fig. 8). Strong localized melting of the ice crust beneath the SPT and other basins as well as ocean crystallization outside these areas also implies continuous mass exchange[2]. Dissipation in the core and associated water flow thus promote efficient rock–water–ice interactions in Enceladus over geological timescales. Only future missions equipped with instruments capable of analysing the organic molecules in the plume[27] with higher accuracy than the Cassini measurements will tell us whether the required conditions have been sustained long enough for life to have emerged on this distant ocean world.

Methods

Core porosity. As a reference for the interior of Enceladus, we consider differentiated interior models consistent with the estimated moment-of-inertia factor (~0.33)[28,29] and with the observed libration (0.120 ± 0.014° or 528 ± 62 m)[2]. Such values suggest that the core of Enceladus has a density of 2,450–2,600 kg m^{-3} and a radius of 185–195 km (see Supplementary Table 1).

Hydrated silicates have densities between 2,580 kg m^{-3} for Mg-serpentine and 3,290 kg m^{-3} for Fe-serpentine (Supplementary Table 2), which is larger than the density of the core. Even w th an amount of iron much lower than chondritic values, the low density of Enceladus core implies considerable poros ty. Assuming that the core is made of serpentine only (the presence of brucite or magnetite would increase the density and therefore the poros ty), we can derive the silicate (sil) density as a function of the amount of iron $x = \mathrm{Fe/Mg}$:

$$\rho_{sil} = \frac{xM_{Fe,ant} + M_{Mg,ant}}{x\frac{\rho_{Mg,ant}}{\rho_{Fe,ant}}M_{Fe,ant} + M_{Mg,ant}}\rho_{Mg,ant} \quad (1)$$

where the molar masses of Fe- and Mg-serpentines (antigorites), $M_{Fe,ant}$ and $M_{Mg,ant}$, respectively, and the corresponding densities are given in Supplementary Table 2. Assuming that the pores are filled with water, the porosity φ is then given by:

$$\varphi = \frac{\rho_{sil} - \rho_b}{\rho_{sil} - \rho_w^0} \quad (2)$$

where ρ_b is the bulk density of the core and ρ_w^0 is the reference density of water (also see values in Supplementary Table 1).

The hydration of the main silicate minerals pyroxene and olivine can produce a variety of combinations between hydrated minerals and hydroxides, described in Supplementary Table 3. End-members are serpentine if (Fe+Mg)/Si = 1.5 (reactions 1A and 1B). For a higher value of this ratio (solar concentration or carbonaceous chondrites give a ratio of 1.9), we use serpentine and brucite without oxidation of iron and therefore no production of H_2 (reactions 2A and 2B), or serpentine and magnetite (reactions 3A, 3B and 3C) with optimum production of H_2.

We have generated porosities for the diversity of mineralogical assemblages described above. As the silicates become more and more hydrated, the poros ty decreases. However, the value of porosity varies between 30 and 20% for chondritic fraction of iron and various degrees of serpentinization. In our models, we consider three values: 0.1, 0.2 and 0.3.

Core permeability. Another bulk property, the permeability, is of paramount importance in investigating porous flow of liquid water. In absence of direct constraints, we consider values representative of granular/fragmented materials such as subglacial tills witnessed beneath flowing glaciers on the Earth's surface: between 10^{-16} m^2 and 10^{-13} m^2 (cf. ref[30]. In order to encompass both this wide range and the values considered by Travis and Schubert[16] in their pioneering study of Enceladus' porous core, we investigated in our calculations the following four values for K: 10^{-15} m^2, 10^{-14} m^2, 10^{-13} m^2 and 10^{-12} m^2.

Core water properties. The density and viscosity of the water flowing in the rock core are variable in our study. We have neglected the mild pressure effect on water density in the temperature and pressure ranges characteristic of Enceladus' porous core and opted instead for a formulation involving a second-order polynomial for T (or, equivalently, a formulation with thermal expansivity that varies linearly with T):

$$\rho_w = 894\ 24 + 1.0807T - 0.0023T^2 \quad (3)$$

with T corresponding to temperature in kelvin. Supplementary Fig. 3 shows that our expression agrees reasonably well with the predictions of the SUPCRT92 software[31], whatever the pressure value. Viscosity is then evaluated using the formulas in ref. [32] from local density and temperature, spanning an interval between 7×10^{-5} and 1.7×10^{-3} Pa s: again, the agreement is satisfactory for the whole pressure range (Supplementary Fig. 3).

As shown in our results, water pressure in the porous core of Enceladus never exceeds the conditions leading to a critical state. However, in our calculations with low permeability ($K \leq 10^{-14}$ m^2), liquid water sometimes reaches the boiling temperature: for numerical reasons, we do not introduce the phase-change effect on density and viscosity; water vapour is described with the density and viscosity values corresponding to liquid water at the boiling temperature for a given pressure. This greatly underestimates the buoyancy of water parcels subjected to vaporization and overestimates their viscosity, which should be kept in mind when analysing these specific cases. Furthermore, the geometry of the porous medium is potentially altered if boiling events are pronounced. Such events would help to maintain the fragmented nature of Enceladus' core.

Enceladus' core: mechanical properties. We consider a wide range of parameters to characterize the strength of the core relative to tidal forcing and the efficiency of tidal friction. The unconsolidated core of Enceladus can be viewed as a highly fragmented material, where tidal deformation is likely to be associated with intergranular friction during grain rearrangements[33,34] or/and frictional sliding along microcracks[35,36]. Both mechanisms depend on the microstructure characteristics (grain distribution, microcrack density), which is unknown in the case of Enceladus.

The mechanical response of such highly fragmented/granular media is classically parameterized using the effective shear modulus, μ_{eff}, and the dissipation function, Q_μ^{-1} (equal to twice the damping ratio, a quantity classically derived in mechanical tests), which control the response amplitude to cyclic tidal forcing and the fraction of mechanical energy that is converted into heat, respectively[18,33–35,37]. An effective viscosity could also be defined assuming a Maxwell rheology as it is classically done when computing tidal deformation in viscoelastic bodies[17,38,39]. However, t is more meaningful to directly represent the dissipation rate as a function of effective shear modulus and dissipation function (or damping ratio) as these are the quantities inferred directly from mechanical tests in the laboratory.

The real and imaginary parts of the complex shear modulus, μ_c, used to compute the tidal deformation, are determined from the effective shear modulus, $\mu_{eff} = |\mu_c|$, and the local dissipation function, Q_μ^{-1}, as follows:

$$\mathrm{Re}(\mu_c) = |\mu_c|\sqrt{1 - \left(Q_\mu^{-1}\right)^2} \quad (4)$$

$$\mathrm{Im}(\mu_c) = |\mu_c| Q_\mu^{-1} \quad (5)$$

The forcing frequency is expected to affect both shear modulus and dissipation function, especially in cohesive unconsolidated materials. The damping ratio (dissipation function) in cohesive soils is expected[40]: (i) to increase at frequencies below 0.1 Hz, due to creep effects of soil skeleton; (ii) to remain more or less constant between 0.1 and 10 Hz; and (iii) to increase at frequencies greater than 10 Hz because of the pore fluid viscosity.

Cyclic loading tests performed on unconsolidated granular materials (mixtures of sands and/or gravels)[35–37,41–43], at low confining pressure, indicate that the effective shear modulus strongly decreases for cyclic strain exceeding 0.01–0.1%, for forcing frequency ranging between typically 0.01 and 1 Hz. These mechanical tests also demonstrate that the damping ratio increases with decreasing shear modulus, and can reach values of about 0.3–0.4, corresponding to dissipation function of 0.6–0.8. Although the occurrence of this reduction of shear modulus (and increase of dissipation) is observed in all samples in laboratory tests[18,34,36], the exact values of cyclic strain at which the change of mechanical behavior occurs may depend on the characteristics of the sample (such as grain-size distribution, composition and porosity), as well as on the frequency and strain history[44,45]. The confining pressure also influences the dissipation rate, but this effect remains moderate[43], at least for confining pressures up to 5 MPa, corresponding to the pressure at the surface of Enceladus' core. Unfortunately, no data exist at higher

© 2017 Macmillan Publishers Limited, part of Springer Nature. All rights reserved.

pressure to confirm this tendency. Even though the conditions inside Enceladus' core are different from those considered in laboratory tests (lower frequency, higher pressure), we assume that a similar trend should occur when the core materials are subjected to cyclic strain. This assumption will have to be confirmed by future mechanical tests in the appropriate range.

In the absence of direct constraints, we can estimate the core mechanical properties from the total power required to explain the global ocean underneath a relatively thin ice shell. By computing the tidal dissipation in the core for a wide range of parameters (see below), we show that the generation of 10–30 GW by tidal friction in Enceladus' unconsolidated core requires an effective shear modulus between 10^7 and 10^8 Pa and a dissipation function between 0.2 and 0.8 (Fig. 1a). This corresponds to a cyclic strain in the core ranging between 0.005 and 0.015% (see Supplementary Fig. 2). According to experimental data on gravelly soils[18,37], the dissipation function typically ranges between 0.05 and 0.2 for such a cyclic strain. As noted above, we anticipate that the dissipation function will be higher at very low frequency ($<10^{-5}$ Hz in the case of tidal deformation for Enceladus) than in these experiments (performed in the range 0.1–1 Hz) because of creep effects in the solid matrix[40]. Although performed on materials of a different nature, such an increase of dissipation (and shear modulus reduction) is observed in mechanical tests performed at very low frequencies (10^{-4}–10^{-3} Hz) on polycrystalline aggregates (olivine[46] or ice[47]). Moreover, the cyclicity of tidalforcing may also result in strain accumulation[44] and gradual build-up of pore pressure[45], favouring the weakness of the core material and maintaining it in a highly deformable state.

Viscoelastic tidal response. Enceladus' interior is divided in three layers, from the centre to the surface: a weak unconsolidated water-saturated porous core, an inviscid water ocean and a viscoelastic ice shell. For simplicity, each layer is assumed to have constant and uniform densities and mechanical properties (see Supplementary Table 4). In the porous core, the complex shear modulus, μ_c, is determined from the effective shear modulus μ_{eff}, equal to the norm of μ_c and the dissipation function Q_μ^{-1}equal to the ratio between the imaginary part and the norm of μ_c. Values between 10^7 and 10^9 Pa and between 0.2 and 0.8 are tested for μ_{eff} and Q_μ^{-1}, respectively. For the outer ice shell, a Maxwell rheology[48] is considered, characterized by constant values of elastic modulus, μ_E, and viscosity, η, throughout the ice shell, ranging between 0.3 and 3.3 GPa and 10^{13} and 10^{18} Pa s, respectively. Thicknesses of the ice shell varying between 2 and 50 km, as well as models with no internal ocean, are tested.

The viscoelastic deformation of Enceladus under the action of periodic tidal forces is computed following the method of ref. [39]. The Poisson equation and the equations of motion are solved for small perturbations in the frequency domain assuming a compressible viscoelastic rheology[39]. The potential perturbation, associated displacement and stress are computed as a function of radius by integrating the radial functions $(y_i)_{i=1,7}$ associated with the radial and tangential displacements (y_1 and y_3, respectively), the radial and tangential stresses (y_2 and y_4, respectively), and the gravitational potential (y_5), and a sixth radial function (y_6) to account for the continuity of the gravitational potential[49] in the elastic equivalent problem. For the deformation of the inviscid water ocean, the static simplified formulation[50] is adopted relying on two radial functions, y_5 and y_7. The solution in the solid part (porous core and ice shell) is expressed as the linear combination of three independent solutions ($y_1 = Ay_{i1} + By_{i2} + Cy_{i3}$), which reduces to one solution in the liquid part. The integration of these three solutions is initiated at the centre using the analytical solutions of spheroidal oscillations for a compressible homogeneous sphere (equations 98, 99 and 100 in ref. [49]). The system of six differential equations is solved by integrating the three independent solutions using a fifth-order Runge–Kutta method with adjustive stepsize control from the centre ($r = 0$ km) to the surface ($r = 252$ km). The three coefficients, A, B and C, are determined at the surface by imposing the boundary conditions appropriate for forcing by an external tidal potential. The solutions for the six radial functions are then computed using the coefficients and the appropriate relationship at each liquid–solid interface[39,49].

From the radial functions, y_1, y_2, y_3 and y_4, and the degree-2 tidal potential, the complex strain and stress tensors are evaluated as a function of radius, latitude and longitude. At each point, the tidal heating rate per unit volume averaged over one tidal cycle is evaluated using: $\bar{h}_{tide} = \frac{\omega}{2}\left[\mathrm{Im}(\sigma_{ij})\mathrm{Re}(\varepsilon_{ij}) - \mathrm{Re}(\sigma_{ij})\mathrm{Im}(\varepsilon_{ij})\right]$ w th ω the orbital angular frequency. The global dissipation is then determined by integrating over the entire volume the dissipation rate computed at each point from the complex strain and stress tensors. In addition, we also determine the global dissipation $\dot{E}_{diss}$ directly from the imaginary part of the complex Love number, k_2^c (defined from the potential radial function, y_5, at the surface ($r = R_s$): $k_2^c = y_5(R_s) - 1$) using the classical formulation[38]: $\dot{E}_{diss} = -\frac{21}{2}\mathrm{Im}(k_2^c)\frac{(\omega R_s)^5}{G}e^2$, where e is the eccentricity. The two approaches are used simultaneously to ensure that the computation is correct. The global dissipation function, Q_μ^{-1}, is defined as $Q_\mu^{-1} = \mathrm{Im}(k_2^c)/|k_2^c|$. The effective cyclic strain is also determined from the second invariant of the strain tensor.

Thermal convection of interstitial water in the porous core. We consider two-phase flow[51,52] of water w thin the rock matrix in the simplified framework of an indeformable saturated solid matrix and w thout phase changes. We also assume uniform porosity φ and permeability K throughout the core. The Boussinesq approximation is considered. The conservation of mass is

$$\nabla \cdot \mathbf{V} = 0 \tag{6}$$

where $\mathbf{V}$ is water velocity. The conservation of momentum for liquid water (Darcy's law) is:

$$\mathbf{V} = -\frac{K}{\eta_w \phi}\left(\nabla p_w - \rho_w \mathbf{g}\right) \tag{7}$$

with η_w being the water viscosity, ρ_w water density, p_w water pressure and $\mathbf{g}$ gravitational acceleration. Permeability K is expected to vary as a function of porosity φ but both are uniform in our models. Assuming a constant core bulk density ρ_b, $\mathbf{g} = -4\pi\rho_b G r \hat{\mathbf{e}}_r$ with $\hat{\mathbf{e}}_r$ a unit vector in the r direction. As a consequence, equation (7) reads:

$$\mathbf{V} = -\frac{K}{\eta_w \phi}\left(\nabla p_w + \frac{4\pi}{3}\rho_b \rho_w G r \hat{\mathbf{e}}_r\right) \tag{8}$$

The conservation of energy involves diffusion of heat in the two-phase medium, advection by water flow and heat production caused by tidal heating H_{tide}:

$$C_b \frac{\partial T}{\partial t} + \phi \rho_w c_w \mathbf{V} \cdot \nabla T = k_b \nabla^2 T + H_{tide} \tag{9}$$

with $C_b = (1-\varphi)c_r\rho_r + \varphi c_w \rho_w$ being bulk volumetric specific heat, c_r and c_w specific heats of rock and water, ρ_r rock density, and k_b bulk thermal conductiv ty, a volume-weighted average of both phases[16,52]. Radiogenic heating is neglected: the mass of the core for parameters listed in Supplementary Table 1 is 6.74×10^{19} kg, so even if we do not account for the presence of water, and assuming the radiogenic content of chondrites CI (3.5 pW kg^{-1})[53], the total radiogenic power is smaller than 0.25 GW at present.

We introduce the following characteristic scales: length $[L] = R_c$, density $[\rho] = \rho_w^0$, viscosity $[\eta] = \eta_w^0$, pressure $[p] = \frac{k_b \eta_w^0}{K C_b}$, temperature $[\Delta T] = \frac{H_{tide} R_c^2}{k_b}$, time $[t] = \frac{C_b R_c^2}{k_b}$. The dimensionless equations corresponding to equations (6), (8) and (9) are

$$\nabla \cdot \mathbf{V} = 0 \tag{10}$$

$$\mathbf{V} = -\frac{1}{\eta_w \phi}\left(\nabla p_w + \gamma \rho_w r \hat{\mathbf{e}}_r\right) \tag{11}$$

$$\frac{\partial T}{\partial t} + \mathcal{C}\phi \rho_w \mathbf{V} \cdot \nabla T = \nabla^2 T + \widetilde{H}_{tide} \tag{12}$$

with $\gamma = \frac{4}{3}\pi \frac{K C_b G \rho_b \rho_w^0 R_c^2}{k_b \eta_w^0}$ being the Rayleigh number, $\mathcal{C} = \frac{\rho_w^0 c_w}{C_b}$ the ratio of volumetric specific heats and $\widetilde{H}_{tide}$ the dimensionless volumetric heating rate (1 in the case of homogeneous heating).

As proposed previously[16], the continuity (equation (10)) and Darcy (equation (11)) equations can be combined to produce the following equation for pressure:

$$\nabla \cdot \left(\frac{1}{\eta_w}(\nabla p_w)\right) = -\gamma \nabla \cdot \left(\frac{\rho_w}{\eta_w} r \hat{\mathbf{e}}_r\right) \tag{13}$$

which is the form solved in our numerical approach.

Equations (11)–(13) are complemented by boundary conditions for pressure and temperature: at the surface of the porous core, a reference value is uniformly prescribed for pressure corresponding for convenience to the dimensionless value associated with this interface in the 1D radial model. In the case of temperature, boundary conditions are time-dependent. A dimensionless value corresponding to 273 K (the ocean temperature in our model) is prescribed when inward advective flux occurs through the interface. In regions where advection of water out of the porous core are predicted, the diffusive heat flux through the surface is set to zero (see Supplementary Section 2.2 for a discussion).

These equations are solved in the framework of the OEDIPUS numerical tool[54,55]: a multigrid method is developed for pressure and an explicit scheme is used for the conservation of energy. Advection terms are treated with a flux-limiter (Superbee) high-resolution method. Owing to the absence of benchmarking efforts for such specific numerical tools, we have validated the program only by computing the value for the onset of convection in the case of an almost planar layer w th basal heating, uniform water viscosity and a linear variation of density with temperature. For numerical reasons, we do not solve the problem in the whole core, down to Enceladus' centre, but in a spherical shell of inner radius r_b=37.2 km corresponding to $f = r_b/R_c = 0.2$. The boundary condition for pressure on this inner sphere ensures the absence of porous flow through this boundary: $\partial p/\partial r = -\gamma \rho_w f$.

Two sets of calculations have been considered (see examples in Supplementary Figures 4 and 5): cases with uniform volumetric heating and cases with a

© 2017 Macmillan Publishers Limited, part of Springer Nature. All rights reserved.

heterogeneous volumetric tidal heating. For each set, we performed 36 calculations corresponding to the thorough investigation of the 3D parameter space: $P_{tide} \times K \times \varphi$ with the global tidal power $P_{tide} \in \{3,10,30,50\}$ GW.

Scaling for thermal vents in the ocean. We follow here the scaling results derived for Europa in refs [56,57] assuming an unstratified and homogeneous subsurface ocean. Consistent with the salt content in icy grains emitted from Enceladus[5], ocean water is assumed to include a sufficient amount of salts in order to provide a positive coefficient for thermal expansion.

The scaling relationships derived in ref. [56] involve three parameters: the natural Rossby number Ro, the Coriolis parameter f' and the ocean's depth H. The Coriolis parameter $f' = 2\Omega\sin\theta$ measures the strength of the influence of the moon's rotation at a given location, with Ω being rotation frequency and θ latitude. In the case of Enceladus, at the poles, $f' = 1.1 \times 10^{-4}\,\mathrm{s}^{-1}$. Similarly, $H \approx 55$ km beneath Enceladus' south pole. The natural Rossby number indicates here the relative height at which the Coriolis effect becomes important: $R_o = \frac{(Bf'^{-3})^{1/4}}{H}$ where $B = \frac{\alpha_o g_o}{\rho_o c_o} F$ is the buoyancy flux (subscript o denotes variables related to the ocean: $\alpha_o = 3 \times 10^{-4}\,\mathrm{K}^{-1}$ is the coefficient of thermal expansion, $g_o \approx 0.12\,\mathrm{m\,s}^{-2}$ the average grav tational acceleration, ρ_o its density and c_o its specific heat; see values in Supplementary Table 1). F is the total power of the seafloor anomaly (in W).

Considering a typical power of 5 GW for polar hotspots (or 1 GW/10 GW respectively) at the seafloor obtained in our simulations (see Fig. 4 in the main text), the Rossby number is 0.008 (or 0.005/0.01 respectively) corresponding to the lower end of the numerical simulations in ref. [57]. According to these simulations, the plume velocity is a few centimetres per second so that the transport from the seafloor to the bottom of the ice shell would be achieved in a month or less.

Such figures are only orders of magnitude. We nevertheless draw attention to the fact that, owing to the combined effects of a thinner ocean (half the thickness of that in Europa), a faster rotation and the polar location of Enceladus main hotspots, the timescale for vertical transport across Enceladus ocean is an order of magnitude smaller than potential Europan equivalents. For this reason, considering a typical vertical transport time of less than a few years for Europa's ocean[57], one should expect a duration of less than a few months for Enceladus' polar vents.

Data availability. The data that support the plots within this paper and other findings of this study are available from the corresponding author upon reasonable request.

Received: 11 May 2017; Accepted: 25 September 2017;
Published online: 06 November 2017

References

1. Thomas, P. C. et al. Enceladus's measured physical libration requires a global subsurface ocean. *Icarus* **264**, 37–47 (2016).
2. Čadek, O. et al. Enceladus's internal ocean and ice shell constrained from Cassini gravity, shape, and libration data. *Geophys. Res. Lett.* **43**, 5653–5660 (2016).
3. Beuthe, M., Rivoldini, A. & Trinh, A. Enceladus's and Dione's fl ating ice shells supported by minimum stress isostasy. *Geophys. Res. Lett.* **43**, 10088–10096 (2016).
4. Le Gall, A. et al. Thermally anomalous features in the subsurface of Enceladus's south polar terrain. *Nat. Astron* **1**, 0063 (2017).
5. Postberg, F. et al. Sodium salts in E-ring ice grains from an ocean below the surface of Enceladus. *Nature* **459**, 1098–1101 (2009).
6. Hsu, H.-W. et al. Ongoing hydrothermal activities within Enceladus. *Nature* **519**, 207–210 (2015).
7. Sekine, Y. et al. High-temperature water–rock interactions and hydrothermal environments in the chondrite-like core of Enceladus. *Nat. Commun* **6**, 8604 (2015).
8. Wa te, J. H. et al. Cassini fi ds molecular hydrogen in the Enceladus plume: evidence for hydrothermal processes. *Science* **356**, 155–159 (2017).
9. Porco, C. C. et al. Cassini observes the active south pole of Enceladus. *Science* **311**, 1393–1401 (2006).
10. Spencer, J. R. et al. Cassini encounters Enceladus: background and the discovery of a south polar hot spot. *Science* **311**, 1401–1405 (2006).
11. Souček, O., Hron, J., Běhounková, M. & Čadek, O. Effect of the tiger stripes on the deformation of Saturn's moon Enceladus. *Geophys. Res. Lett.* **43**, 7417–7423 (2016).
12. Běhounková, M., Souček, O., Hron, J. & Čadek, O. Plume activity and tidal deformation on Enceladus influenced by faults and variable ice shell thickness. *Astrobiology* **17**, 941–954 (2017).
13. McKinnon, W. B. The shape of Enceladus as explained by an irregular core: implications for gravity, libration, and survival of its subsurface ocean. *J. Geophys. Res.* **118**, 1775–1788 (2013).
14. Monteux, J., Collins, G. S., Tobie, G. & Choblet, G. Consequences of large impacts on Enceladus' core shape. *Icarus.* **264**, 300–310 (2016).
15. Neveu, M. & Rhoden, A. R. The origin and evolution of a differentiated Mimas. *J. Geophys. Res.* **296**, 183–196 (2015).
16. Travis, B. J. & Schubert, G. Keeping Enceladus warm. *Icarus* **250**, 32–42 (2015).
17. Roberts, J. H. The fluffy core of Enceladus. *Icarus* **258**, 54–66 (2015).
18. Rollins, K. M., Evans, M. D., Diehl, N. B. & Daily, W. D. Shear modulus and damping relationships for gravels. *J. Geotech. Geoenviron. Eng* **124**, 396–405 (1998).
19. Hedman, M. M. et al. An observed correlation between plume activ ty and tidal stresses on Enceladus. *Nature* **500**, 182–184 (2013).
20. Nimmo, F., Porco, C. C. & Mitchell, C. Tidally modulated eruptions on Enceladus: Cassini ISS observations and models. *Astron. J.* **148**, 46 (2014).
21. Běhounkovà, M. et al. Timing of water plume eruptions on Enceladus explained by interior viscosity structure. *Nat. Geosci* **8**, 601 (2015).
22. Monnereau, M. & Dubuffet, F. Is Io's mantle really molten? *Icarus* **158**, 450–459 (2002).
23. Soderlund, K. M., Schmidt, B. E., Wicht, J. & Blankenship, D. D. Ocean-driven heating of Europa's icy shell at low latitudes. *Nat. Geosci* **7**, 16–19 (2014).
24. Grannan, A. M., Favier, B., Le Bars, M. & Aurnou, J. M. Tidally forced turbulence in planetary interiors. *Geophys. J. Int.* **208**, 1690–1703 (2016).
25. Lainey, V. et al. New constraints on Saturn's interior from Cassini astrometric data. *Icarus* **281**, 286–296 (2017).
26. Fuller, J., Luan, J. & & Quataert, E. Resonance locking as the source of rapid tidal migration in the Jup ter and Saturn moon systems. *Mon. Not. R. Astr. Soc.* **458**, 3867–3879 (2016).
27. Postberg, F. et al. The E ring in the vicinity of Enceladus. II. Probing the moon's interior—the composition of E-ring particles. *Icarus* **193**, 438–454 (2008).
28. Iess, L. et al. The gravity fi ld and interior structure of Enceladus. *Science* **344**, 78–80 (2014).
29. McKinnon, W. B. Effect of Enceladus's rapid synchronous spin on interpretation of Cassini gravity. *Geophys. Res. Lett.* **42**, 2137–2143 (2015).
30. Fountain, A. G. & Walder, J. S. Water fl w through temperate glaciers. *Rev. Geophys.* **36**, 299–328 (1998).
31. Johnson, J. W., Oelkers, E. H. & Helgeson, H. C. SUPCRT92: a software package for calculating the standard molal thermodynamic properties of minerals, gases, aqueous species, and reactions from 1 to 5000 bar and 0 to 1000 °C. *Chem. Geol.* **18**, 899–947 (1992).
32. Johnson, J. W. & Norton, D. Critical phenomena in hydrothermal systems; state, thermodynamic, electrostatic, and transport properties of H_2O in the critical region. *Am. J. Sci.* **291**, 541–648 (1991).
33. Ishibashi, I. & Zhang, X. Unifi d dynamic shear moduli and damping ratios of sand and clay. *Soils Found.* **33**, 182–191 (1993).
34. Fiscina, J. E. et al. Dissipation in quasistatically sheared wet and dry sand under confi ement. *Phys. Rev. E* **86**, 020103 (2012).
35. Wulff, A. M., Hashida, T., Watanabe, K. & Takahashi, H. Attenuation behaviour of tuffac ous sandstone and granite during microfracturing. *Geophys. J. Int.* **139**, 395–409 (1999).
36. Brennan, A. J., Thusyanthan, N. I. & Madabhushi, S. P. Evaluation of shear modulus and damping in dynamic centrifuge tests. *J. Geotech. Geoenviron. Eng* **131**, 1488–1497 (2005).
37. Seed, H. B., Wong, R. T., Idriss, I. M. & Tokimatsu, K. Moduli and damping factors for dynamic analyses of cohesionless soils. *J. Geotech. Geoenviron. Eng* **112**, 1016–1032 (1986).
38. Segatz, M., Spohn, T., Ross, M. N. & Schubert, G. Tidal dissipation, surface heat fl w, and figu e of viscoelastic models of Io. *Icarus* **75**, 187–206 (1988).
39. Tobie, G., Mocquet, A. & Sotin, C. Tidal dissipation within large icy satellites: Appli- cations to Europa and Titan. *Icarus* **177**, 534–549 (2005).
40. Shibuya, S., M tachi, T., Fukuda, F. & Degoshi, T. Strain rate effects on shear modulus and damping of normally consolidated clay. *Geotech. Test. J.* **18**, 365–375 (1995).
41. Sun, J. I., Golesorki, R. & Seed, H. B. *Dynamic Moduli and Damping Ratios for Cohesive Soils*. (Earthquake Engineering Research Center, Univ, California, Berkeley, 1988). Report no. UCB/EERC-88/15.
42. Araei, A. A., Razeghi, H. R., Tabatabaei, S. H. & Ghalandarzadeh, A. Loading fre- quency effect on stiffness, damping and cyclic strength of modeled rockfill materials. *Soil Dyn. Earthq. Eng.* **33**, 1–18 (2012).
43. Zhou, W., Chen, Y., Ma, G., Yang, L. & Chang, X. A modifi d dynamic shear modulus model for rockfill materials under a wide range of shear strain amplitudes. *Soil Dyn. Earthq. Eng* **92**, 229–238 (2017).
44. Wichtmann, T., Niemunis, A. & Triantafyllidis, T. Strain accumulation in sand due to cyclic loading: drained triaxial tests. *Soil Dyn. Earthq. Eng* **25**, 967–979 (2005).
45. Raad, L., Minassian, G. H. & Gartin, S. Characterization of saturated granular bases under repeated loads. *Transp. Res. Rec.* **369**, 73–82 (1992).
46. Faul, U. H. & Jackson, I. The seismological signature of temperature and grain size variations in the upper mantle. *Earth Planet. Sci. Lett.* **234**, 119–134 (2005).

© 2017 Macmillan Publishers Limited, part of Springer Nature. All rights reserved.

47. Cole, D. M. A model for the anelastic straining of saline ice subjected to cyclic loading. *Phil. Mag. A* **72**, 231–248 (1995).
48. Castillo-Rogez, J. C., Efroimsky, M. & Lainey, V. The tidal history of Iapetus: spin dynamics in the light of a refi ed dissipation model. *J. Geophys. Res.* **116**, E09008 (2011).
49. Takeushi H., Saito M. in *Methods in Computational Physics* Vol. 1 (ed. Bolt, B. A.) 217–295 (Academic, New York, 1972).
50. Saito, M. Some problems of static deformation of the Earth. *J. Phys. Earth* **22**, 123–140 (1974).
51. Ricard, Y. in *Mantle Dynamics*. *Treatise on Geophysics* Vol. 7 (ed. Schubert, G.) 23–71 (Elsevier, Amsterdam, The Netherlands, 2015).
52. Kalousová, K., Souček, O., Tobie, G., Choblet, G. & Čadek, O. Ice melting and down- ward transport of meltwater by two-phase fl w in Europa's ice shell. *J. Geophys. Res.* **119**, 532–549 (2014).
53. Palme, H. & O'Neill, H. S. C. in *Mantle and Core. Treatise on Geochemistry* Vol. 2 (ed. Carlson, R. W.) 1–38 (Elsevier, Amsterdam, The Netherlands, 2003).
54. Choblet, G. Modelling thermal convection with large viscosity gradients in one block of the cubed sphere. *J. Comput. Phys.* **205**, 269–291 (2005).
55. Choblet, G., Čadek, O., Couturier, F. & Dumoulin, C. ŒDIPUS: a new tool to study the dynamics of planetary interiors. *Geophys. J. Int* **170**, 9–30 (2007).
56. Goodman, J. C., Collins, G. C., Marshall, J. & Pierrehumbert, R. T. Hydrothermal plume dynamics on Europa: implications for chaos formation. *J. Geophys. Res.* **109**, E03008 (2004).
57. Goodman, J. C. & Lenferink, E. Numerical simulations of marine hydrothermal plumes for Europa and other icy worlds. *Icarus* **221**, 970–983 (2012).

Acknowledgements

The research leading to these results received financial support from the CNRS PICS (G.C., G.T.), the CNRS-INSU PNP program (G.C., G.T.) and the ANR OASIS project (G.C., G.T.), from the Czech Science Foundation project 15-14263Y (OS), from the German Research Foundation DFG projects PO 1015/2-1, /3-1, /4-1 (F.P.) and from the Icy Worlds node of NASA's Astrobiology Institute 13-NAI7-0024 (C.S.). The computations were carried out using CCIPL computational facilities (France).

Author contributions

All authors contributed to the discussions and commented on the manuscript. G.C. and G.T. led the writing of the letter. C.S. performed calculations on core porosity. G.T. computed the tidal dissipation in the porous core. G.C. developed the 3D code of porous water flow and conducted the numerical simulations of porous convection. All authors contributed to the interpretation of results.

Competing Interests

The authors declare no competing financial interests.

Additional information

Supplementary information is available for this paper at https://doi.org/10.1038/s41550-017-0289-8.

Reprints and permissions information is available at www.nature.com/reprints.

Correspondence and requests for materials should be addressed to G.C.

Publisher's note: Springer Nature remains neutral with regard to jurisdictional claims in published maps and institutional affiliations.

© 2017 Macmillan Publishers Limited, part of Springer Nature. All rights reserved.